

# Terahertz electromagnetic field propagation in human tissues: a study on communication capabilities

G. Piro<sup>1</sup>, P. Bia<sup>1</sup>, G. Boggia<sup>1</sup>, D. Caratelli<sup>2</sup>, L. A. Grieco<sup>1</sup>, L. Mescia<sup>1</sup>

<sup>1</sup>*DEI, Politecnico di Bari, Via Orabona 4, 70125, Bari, Italy*

<sup>2</sup>*The Antenna Company Nederland B.V., High Tech Campus, Eindhoven, The Netherlands*

---

## Abstract

A Body Area Nano-NETwork represents a system of biomedical nano-devices that, equipped with sensing, computing, and communication capabilities, can be implanted, ingested, or worn by humans for collecting diagnostic information and tuning medical treatments. The communication among these nano-devices can be enabled by graphene-based nano-antennas, which generate electromagnetic waves in the Terahertz band. However, from a perspective of the electromagnetic field propagation, human tissues generally introduce high losses that significantly impair the communication process, thus limiting communication ranges. In this context, the aim of this contribution is to study the communication capabilities of a Body Area Nano-NETwork, by carefully taking into account the inhomogeneous and disordered structure offered by biological tissues. To this end, the propagation of Pulsed Electric Fields in a stratified media stack made up by stratum corneum, epidermis, dermis, and fat has been carefully modeled. First, electric and magnetic fields, as well as the Poynting vector, have been calculated through an accurate Finite-Difference Time-Domain dispersive modeling based on the fractional derivative operator. Second, path loss and molecular absorption noise temperature have been evaluated. Finally, channel capacity and the related transmission ranges have been estimated by using some baseline physical interfaces. Moreover, the comparison with respect to reference values already available in the literature is presented too. Obtained results clearly highlight that new research efforts are needed to ensure the considered communications due to the severe impairment suffered by electromagnetic

waves.

*Keywords:* Body Area Nano-NETworks, nanoscale communications, Pulsed Electric Fields, propagation models, channel capacity, Fractional Calculus, Finite-difference Time-Domain

---

## 1. Introduction

Medical applications continuously evolve thanks to technological advancements. For instance, thanks to the numerous contributions of Information and Communications Technology (ICT), it is now possible to envisage a pervasively  
5 monitoring of biological functionalities of people through a network of on-body sensing devices, forming a Body Area Network (BAN), and to support advanced healthcare services, ambient assisted living, sport training, streaming, emergency, computer vision, wearable health monitoring, sleep staging, and telemedicine applications [1, 2, 3]. Instead, more recently, the innovation process  
10 triggered by the nanotechnology is laying the foundation for a substantial revolution of healthcare monitoring systems, by collecting biological data directly from the inner human body, i.e., by using nanometric sensing units. In fact, it is foreseen that biomedical nano-devices can be implanted, ingested, or worn by humans for collecting diagnostic information (e.g., the presence of sodium, glu-  
15 cose, and/or other ions in blood, cholesterol, as well as cancer biomarkers and other infectious agents) and for tuning medical treatments (e.g., administration of insulin and other drugs through under-skin actuators) [4, 5, 6, 7]. Given the limited size of nano-devices (i.e., in the order of hundreds of nanometers), the resulting networked system is generally referred to as Body Area Nano-  
20 NETwork (BANNET) [8, 9].

The literature, already demonstrated the communication feasibility at the nanoscale by the adoption of graphene-based nano-antennas generating electromagnetic waves in the Terahertz band (i.e., from 0.1 THz to 10 THz) [10, 11]. When considering the propagation in the air medium, Terahertz commu-  
25 nications reach very high physical data rates (i.e., more than 1 Tbps) and trans-

mission distances in the order of few tens of millimeters [12, 13]. Human tissues, instead, introduce high losses that significantly impair the communication process, entailing lower physical transmission rates and lower communication ranges [11, 14, 15]. There exist, in fact, many phenomena (like absorption by  
30 molecules and scattering by different kind of cells) that make the propagation of electromagnetic waves extremely challenging in this kind of media [16].

In this context, it is widely recognized that the electromagnetic field propagation inside biological tissues is significantly influenced by a disordered structure at both macroscopic and mesoscopic scale, which provokes a variability of the  
35 dielectric permittivity in both spatial and frequency domain. What however remains surprising is that at the time of this writing, and for the best of authors' knowledge, all the available studies (including those presented in [11], [14], and [15]) simply focus on a non-dispersive and spatially homogeneous medium (like skin, blood, or fat). Accordingly, the presented findings may be quite different  
40 with respect to the actual ones.

Based on these premises, the present contribution provides an important step forwards for the state of the art, by formulating a more accurate study of in-body electromagnetic communications, which carefully considers the impact of a dispersive model of human tissues. Specifically, the novelty of this paper  
45 is the development of a sophisticated channel model, that takes into account the spatial dependence of the skin permittivity has been modeled by means of a stack of different homogeneous media. This represents the novelty The reference use case addressed in this paper is depicted in Figure 1. It assumes the presence of two communicating nano-devices: the source node is located outside of the  
50 arm, but directly attached to the human body; the destination device, instead, is implanted inside the body.

In summary, the conducted study aims at characterizing the Pulsed Electric Field (PEF) propagation in a stratified media stack made up by stratum corneum, epidermis, dermis, and fat. First of all, an accurate Finite-Difference  
55 Time-Domains (FDTDs) dispersive modeling based on the fractional derivative operator, has been used to (i) numerically solve the Maxwell's equations di-

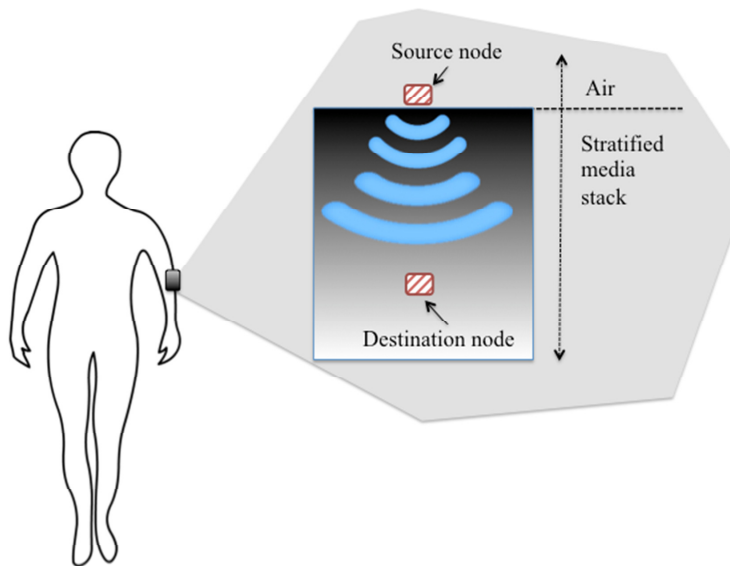


Figure 1: Sketch of the investigated use case.

rectly in the time domain and (ii) to calculate the electromagnetic field and the Poynting vector as a function of the time and the distance between source and destination devices. Second, the losses due to both spreading and absorp-  
 60 tion processes, as well as the molecular absorption noise temperature, have been evaluated in the frequency domain as a function of the distance between communicating node pair. Finally, reference transmission schemes recently conceived in the context of nanoscale communications [12] have been used for estimating communication capabilities in a BANNET, in terms of channel capacity and  
 65 related transmission ranges. The comparison with respect to reference results already available in the literature (i.e., those reported in [11],[14], and [15]) and referring to homogeneous media has been also provided. Obtained results demonstrate that:

- the channel capacity reduces in human tissues in comparison with the air;
- 70 • achieved results significantly differ from those available in the literature and obtained by considering a simplified model for human tissues, based on homogeneous media;

- a physical data rate in the order of Terabit per second can be only reached for transmission ranges less than 2 mm;
- 75 • when the distance between source and destination nodes exceeds 9 mm, communication capabilities are extremely impaired (i.e., the physical data rate is lower than 1 bps).

To conclude, the rest of the paper is organized as it follows. In Section 2, the accurate PEF propagation model related to the stratified media stack, the re-  
80 sulting path loss, and the molecular absorption noise temperature are presented. The procedure used to evaluate the channel capacity and the related transmission ranges, as well as obtained results, are discussed in Section 3. Finally, Section 4 draws the conclusions and presents some future research activities.

## 2. Terahertz propagation model

85 The modeling of PEFs propagation in biological tissues has become a topic of increasing interest for research activities in bioelectric, a new interdisciplinary field combining knowledge of electromagnetic theory, modeling and simulations, physics, material science, cell biology, and medicine [17, 18, 19]. In particular, beside a variety of therapeutic and diagnostic applications, the feasibility of  
90 PEFs and transient phenomena, in radio frequency, mm-wave, and Terahertz band, could be successfully applied in the field of remotely-powered implantable devices to calculate the range of frequency optimizing the trade-off between the received power and tissue absorption [14, 20].

Generally, the complex heterogeneous, inhomogeneous and disordered struc-  
95 ture of biological tissues at both microscopic and mesoscopic scale results in a frequency dispersion of the macroscopic dielectric response. As a consequence, accurate theoretical models and simulation tools are essential to model realistic PEFs propagation, loss values, temperature changes, current densities and pathways inside the biological media over broad frequency range [21, 22, 23].  
100 Moreover, they are invaluable tools to better understand the physical phenom-

ena involved during the interaction of PEFs at cellular, molecular, organs and whole body level.

### 2.1. Dielectric dispersion model

The dielectric properties of biological tissues strongly depend on the bound water content. In particular, the dielectric response in frequency domain of tissues having high water content can be described by a Debye model [24], i.e. a simple exponential expression with a single relaxation time. The disordered nature and microstructure of biological matter as well as the supracellular organization in such materials, often taking the form of fractal structures, trigger different polarization mechanisms which induce multiple relaxation times and a non-symmetric time-domain response. As result, the experimental dielectric response in frequency domain usually cannot be modeled by an exponential law based on Debye-type dispersion or combination of such dispersions, and more complex empirical dispersion functions have to be taken into account. Thus, in order to model realistic electromagnetic wave propagation over broad frequency range and the multi-relaxation phenomena, the complex permittivity of each biological tissue,  $\varepsilon_r$ , has been modeled using the following Havriliak-Negami relationship:

$$\varepsilon_r = \varepsilon'_r - j\varepsilon''_r = \varepsilon_{r\infty} + \sum_{p=1}^N \frac{\Delta\varepsilon_{r_p}}{[1 + (j\omega\tau_p)^{\alpha_p}]^{\beta_p}} - j \frac{\sigma}{\omega\varepsilon_0}, \quad (1)$$

where  $\omega = 2\pi f$  is the angular frequency,  $\varepsilon_{r\infty}$  is the relative permittivity for  $\omega \rightarrow +\infty$ ,  $\Delta\varepsilon_{r_p}$  and  $\tau_p$  are the amplitude change and relaxation time of the  $p$ -th relaxation process,  $N$  is the number of relaxation processes,  $\sigma$  is the static ionic conductivity,  $0 \leq \alpha_p, \beta_p \leq 1$  are heuristically derived power-law exponents, and  $\varepsilon_0$  is the free space permittivity.

The main constituent of the healthy human skin is the free water (around 70% by weight). The remaining 30% is the biological background material mainly composed by bound water, keratin, lipids and collagen. As result, the interaction of electromagnetic field with skin at the Terahertz band can be investigated by considering the propagation inside the effective medium resulting

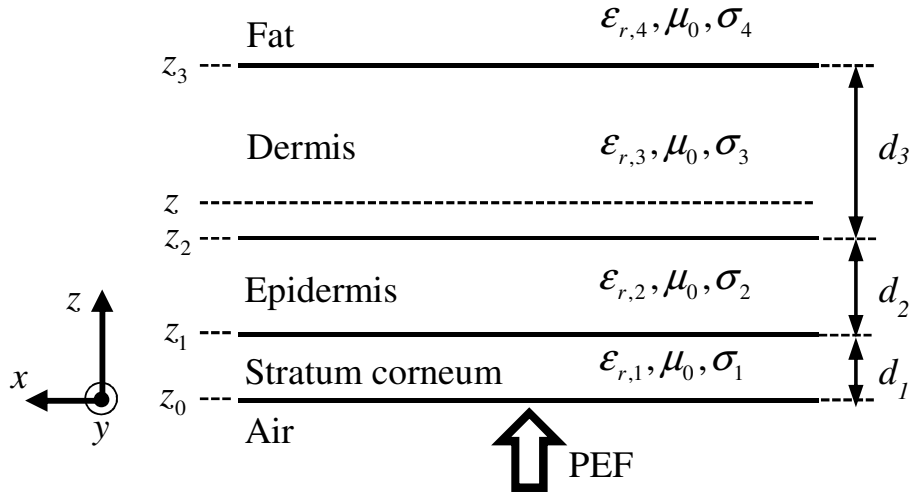


Figure 2: The considered layered structure.

by the binary mixture of water and biological background material. Most recent  
115 studies of electromagnetic channel at the Terahertz band for the body-centric  
nano-networks are based on such an approach treating the skin tissue as a  
homogeneous semi-infinite medium [14, 20]. Unfortunately, the water concen-  
tration in the binary mixture varies in a complex way. As a consequence, a  
semi-infinite effective slab model employing an average water content would not  
120 correctly predict the behavior of Terahertz electromagnetic waves propagation  
in human skin. To this aim, a non-homogeneous model of the skin tissue based  
on stratified media stack has been taken into account. It consists of stratum  
corneum, epidermis, dermis and fat, as in the schematic diagram is Figure 2.

The dielectric properties of stratum corneum, epidermis, dermis and fat in  
a desired frequency range, as well as the thickness of each layer have been  
calculated by considering experimental results reported in the literature [25, 26,  
27, 28]. In particular, the permittivity has been interpolated through Eq. (1),  
by minimizing the following error function:

$$\text{err} = \frac{\int_{\omega_{\min}}^{\omega_{\max}} |\epsilon_{r,\text{exp}}(\omega) - \epsilon_r(\omega)|^2 d\omega}{\int_{\omega_{\min}}^{\omega_{\max}} |\epsilon_{r,\text{exp}}(\omega)|^2 d\omega} \leq \delta, \quad (2)$$

where  $\delta$  is the maximum tolerable error,  $\epsilon_{r,\text{exp}}$  is the measured permittivity, and  
125  $\epsilon_r$  represents the general Havriliak-Negami dielectric response.

The set of parameters related to each layer of the considered stratified media stack have been reported in Table 1. These values have been obtained by using Eq. (2) in a bandwidth ranging from 0.5 THz to 1.5 THz (i.e., the one considered in our study, as described in Section 3) and by setting  $N = 2$ .

Table 1: Havriliak-Negami parameters of the recovered complex permittivity function

Parameter	Stratum Corneum	Epidermis	Dermis	Fat
$\alpha_1$	1	0.95	0.92	1
$\alpha_2$	-	-	0.97	0.89
$\beta_1$	1	0.96	0.8	0.78
$\beta_2$	-	-	0.99	0.90
$\tau_1$ (ps)	15.9	15.9	1.6	2.3
$\tau_2$ (ns)	-	-	159	15.9
$\Delta\epsilon_{\tau_1}$	12.22	89.61	5.96	1.14
$\Delta\epsilon_{\tau_2}$	-	-	380.4	9.8
$\sigma$ (S/m)	0.035	0.01	0.1	0.035
$\epsilon_{r\infty}$	2.4	3	4	2.5
$d$ (mm)	$30 \times 10^{-3}$	0.35	1	$\infty$

## 130 2.2. Fractional-Calculus-Based FDTD method

The full wave FDTD method is the most recognized, powerful and efficient numerical technique which solves Maxwell's equations directly in the time domain. Due to its simplicity, low computational footprint as well as its capability to model in a straight-forward and effective way many type of dispersive media,  
135 FDTD method is widely utilized for simulating the propagation of electromagnetic waves and their interaction with biological media. Taking into account that the Havriliak-Negami relationship includes fractional powers of angular frequency  $j\omega$ , the design of the FDTD algorithm requires special treatments. In fact, the approximation of fractional derivatives has to be embedded into the  
140 simulator. To this aim, a FDTD scheme based on Riemann-Liouville theory of



fractional differentiation has been derived. In particular, in combination with the basic time-marching scheme, it directly incorporates a series representation of the Riemann-Liouville fractional derivative operator, the multiple relaxation times and ohmic losses occurring in biological media, as well as a dedicated  
145 uniaxial perfectly matched layer boundary conditions. In particular, applying a second order accurate finite-difference scheme and the procedure detailed in appendix section for the finite-difference discretization, the the electric field,  $\mathcal{E}$ , and the magnetic field  $\mathcal{H}$  can be calculated in detail.

The electromagnetic source is a plane wave propagating along the positive z-direction with electric field linearly polarized along the x-axis. In particular, the time-domain signal source is an electric current density  $\mathcal{J}_0$  placed at a given position  $z = \bar{z}$  inside the computational domain:

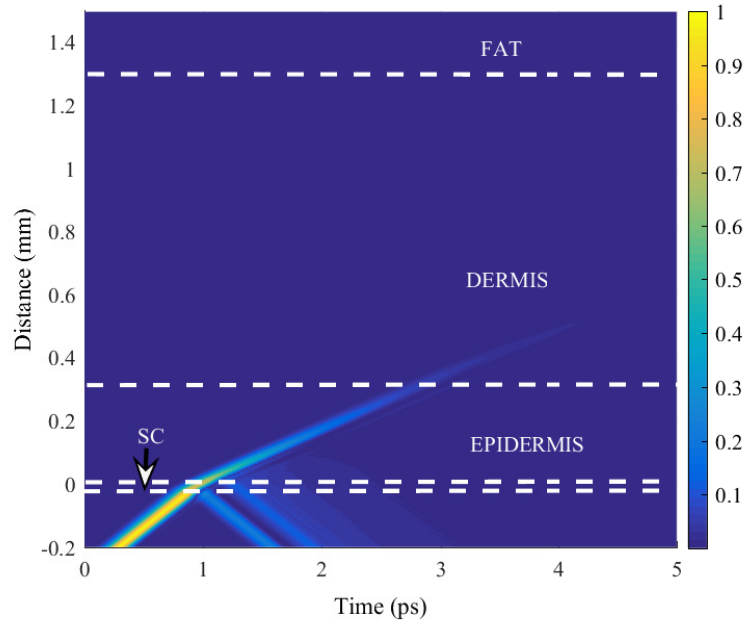
$$\mathcal{J}_0(z, t) = \exp\left\{-a^2\left(t - \frac{2}{a}\right)^2\right\} \sin\left[2\pi f_0\left(t - \frac{4}{a}\right)\right] \delta(z - \bar{z}) \hat{\mathbf{x}}, \quad (3)$$

where the parameters  $f_0 = 1$  THz and  $1/a = 100$  fs have been selected to achieve  
150 a bandwidth from 0.5 THz to 1.5 THz. The considered time and spatial steps are  $\Delta t = 10$  fs and  $\Delta z = 6$   $\mu\text{m}$ , respectively. The validation of the developed numerical procedure has been illustrated in detail in our previous papers [21, 22, 23]. In particular, numerical results have been presented for various test cases and compared with those calculated by using a fully analytical approach based  
155 on the analytical Fourier transform. There reference contributions demonstrate the accuracy of the proposed FDTD method in the study of broadband wave propagation in complex and stratified dispersive media.

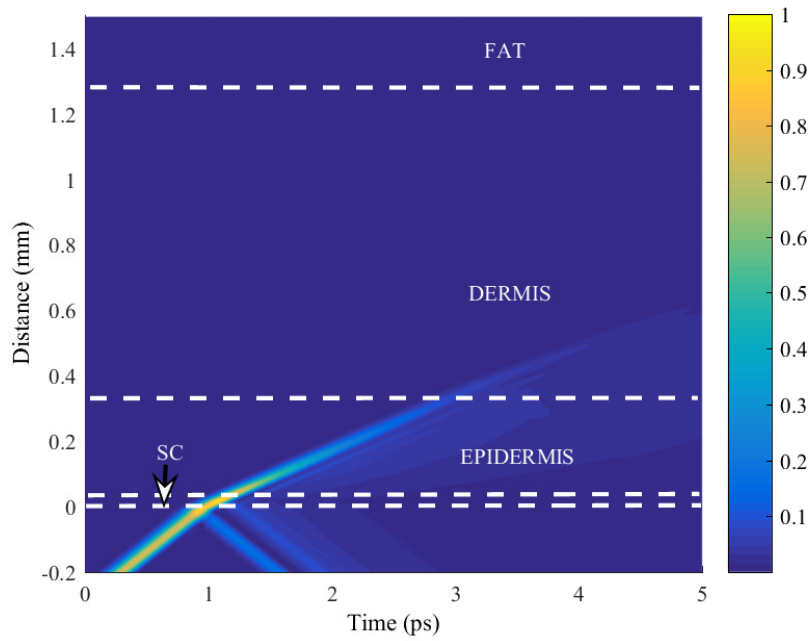
Figures 3.(a) and 3.(b) show the modulus of the normalized electric field,  $\mathcal{E}$ , and the magnetic field,  $\mathcal{H}$ , respectively, as a function of the time and the distance  
160 between source and destination nodes. Many details about the analytical model used to calculate  $\mathcal{E}$  and  $\mathcal{H}$  have been discussed in the Appendix.

To provide a further insight, the Poynting vector,  $\mathbf{S}(\omega, z)$ , is also reported in Figure 4. In particular, it has been calculated as:

$$\mathbf{S}(\omega, z) = \mathbf{E} \times \mathbf{H}^*,$$



(a)



(b)

Figure 3: Modulus of the normalized space-time distribution of (a) electric field, (b) magnetic field.

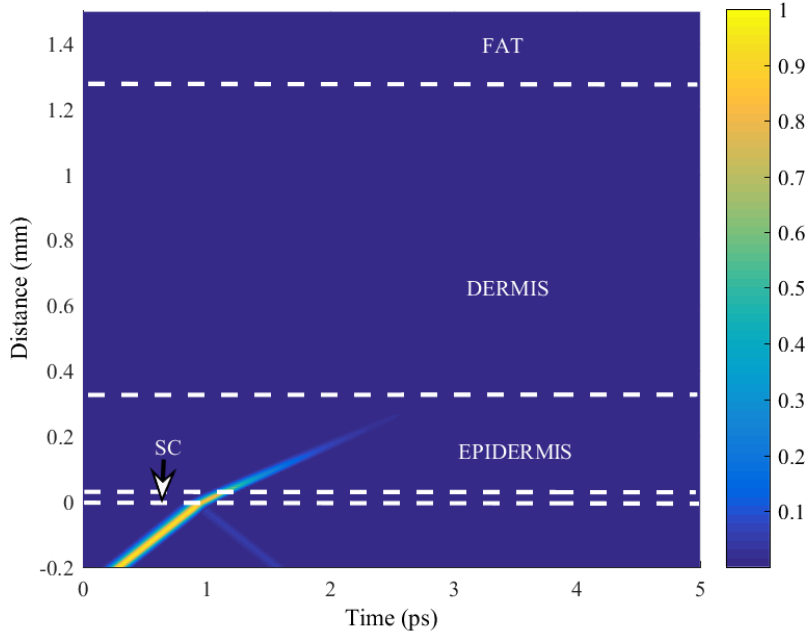


Figure 4: Modulus of the normalized space-time distribution of Poynting vector.

$\mathbf{E}$  and  $\mathbf{H}$  are the Fourier transform of  $\mathcal{E}$  and  $\mathcal{H}$ , respectively.

In Figures 3-4, it can be observed the multiple reflected waves generated by the stratified media stack as well as the main reflection phenomenon occurring at the air-skin interface. Moreover, it is evident the wave pulse spreading due to the propagation inside the dispersive biological media.

### 2.3. Path loss model and Noise power spectral density

Let  $A(\omega, \tilde{z})$  be the total path loss of PEFs traveling inside the considered layered system. It is due to both spreading and absorption effects:

$$A(\omega, \tilde{z}) \Big|_{\text{dB}} = A_s(\omega, \tilde{z}) \Big|_{\text{dB}} + A_a(\omega, \tilde{z}) \Big|_{\text{dB}}, \quad (4)$$

where  $\tilde{z} = z - z_0$  is the total path length,  $z_0$  being the  $z$ -coordinate of the reference section,  $A_s$  and  $A_a$  are the spreading path loss and absorption path loss due to the expansion of a wave and molecular absorption in the biological tissue, respectively.

The spreading path loss is generated by the expansion of waves in human tissues. It can be defined as:

$$A_s(\omega, \tilde{z}) \Big|_{\text{dB}} = 20 \log \left( 4\pi \int_{z_0}^z \frac{dz}{\lambda_g(\omega, z)} \right) \quad (5)$$

where

$$\lambda_g(\omega, z) = \begin{cases} \lambda_{g,1}(\omega, z) & 0 \leq z \leq z_1 \\ \lambda_{g,2}(\omega, z) & z_1 \leq z \leq z_2 \\ \lambda_{g,3}(\omega, z) & z_2 \leq z \leq z_3 \\ \lambda_{g,4}(\omega, z) & z \geq z_3 \end{cases} \quad (6)$$

and

$$\lambda_{g,k} = \frac{\lambda_0}{\sqrt{\frac{\varepsilon'_{r,k}}{2} \left[ \sqrt{1 + \left( \frac{\varepsilon''_{r,k}}{\varepsilon'_{r,k}} + \frac{\sigma_k}{\omega \varepsilon_0 \varepsilon'_{r,k}} \right)^2} + 1 \right]}} \quad k = 1, 2, 3, 4 \quad (7)$$

is the wavelength of the plane wave propagating in the  $k$ -th lossy media and  $\lambda_0$  is the free-space wavelength.

The absorption path loss, instead, is due to the absorption of human tissues. It is defined as:

$$A_a(\omega, \tilde{z}) \Big|_{\text{dB}} = 10 \log \frac{\mathbf{S}(\omega, z)}{\mathbf{S}(\omega, z_0)} \quad (8)$$

where  $\mathbf{S}(\omega, z)$  is the Poynting vector, as defined in the previous subsection.

175 Figures 5, 6, and 7 show the spreading path loss, the absorption path loss, and the total path loss, respectively. As expected, the Terahertz band is frequency-selective and propagation losses increase with both frequency and distance between source and destination nodes. Nevertheless, the obtained results clearly show that the total path loss is mainly influenced by absorption  
180 phenomena, which are able to generate a loss up to 6 times higher than the one introduced by the expansion of waves.

As already described in [15], the noise power spectral density,  $N(\omega, \tilde{z})$ , is mainly influenced by the molecular absorption. Therefore, given  $T_{\text{eq}}(\omega, \tilde{z})$  the

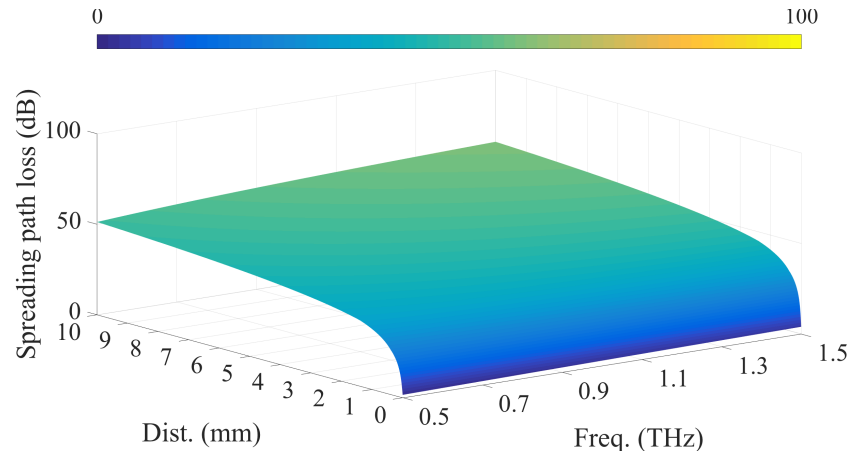


Figure 5: Spreading path loss.

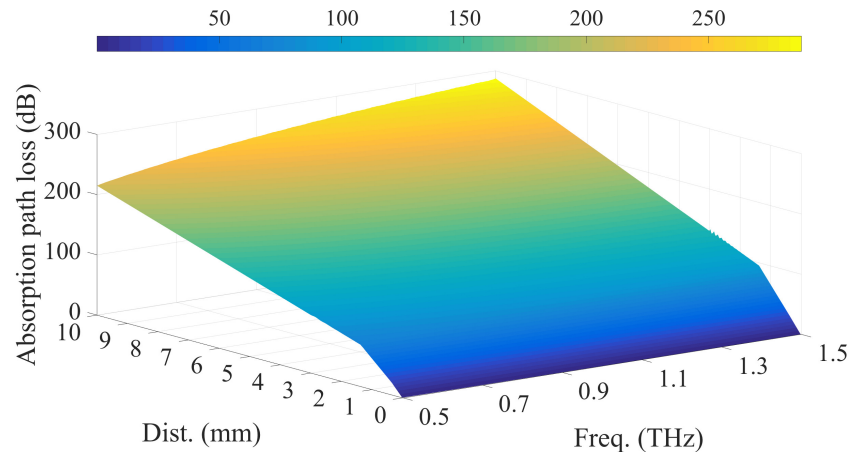


Figure 6: Absorption path loss.

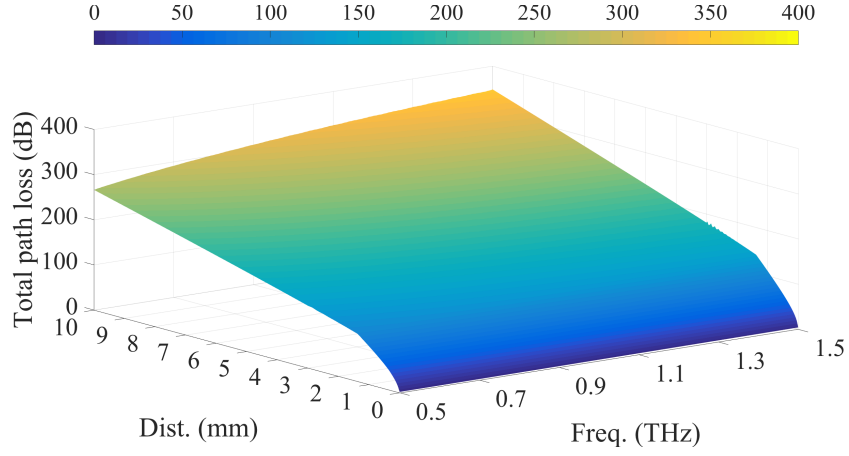


Figure 7: Total path loss.

equivalent noise temperature due to molecular absorption, it can be computed as:

$$N(\omega, \tilde{z}) = k_B T_{\text{eq}}(\omega, \tilde{z}), \quad (9)$$

where  $k_B$  is the Boltzmann constant.

According to [20], the equivalent noise temperature due to molecular absorption can be computed as:

$$T_{\text{eq}}(\omega, \tilde{z}) = T_0 \left[ 1 - \frac{\mathbf{S}(\omega, z)}{\mathbf{S}(\omega, z_0)} \right] \quad (10)$$

where  $T_0 = 310$  K is the normal body temperature and  $\mathbf{S}(\omega, z)$  is the Poynting vector. It is important to remark that the equivalent noise temperature is  
 185 mainly caused by the molecular internal vibration. In particular, during the propagation inside the lossy biological medium, the electromagnetic field is absorbed and a part of its energy is converted to heat. As result, the equivalent noise temperature shows a frequency and distance dependence since it maintains the same dependence of the propagation losses. This occurrence is modeled by  
 190 the term  $1 - \mathbf{S}(\omega, z)/\mathbf{S}(\omega, z_0)$ , which describe the channel emissivity.

From Figure 8, it is also worthwhile to note that equivalent noise temperature increases with the distance. Indeed, the electromagnetic field is mainly

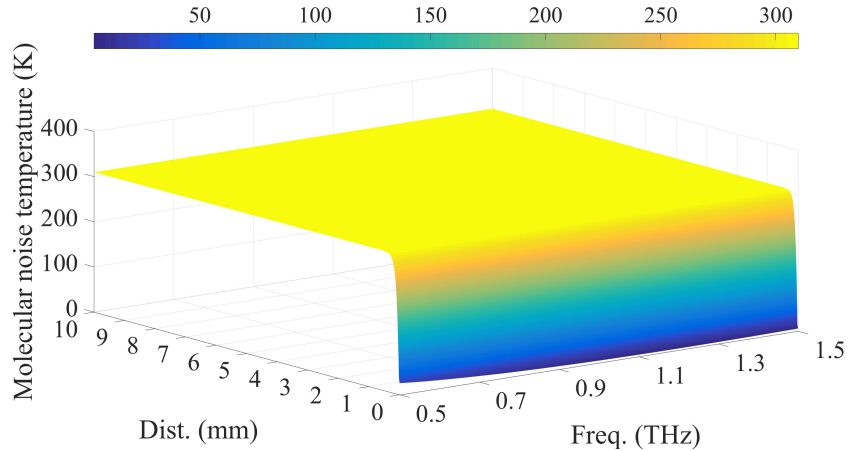


Figure 8: Molecular absorption noise temperature

absorbed within the skin layers and at the level of millimeters (i.e., inside the fat) the whole medium transmissivity can be neglected. As result, the molecular noise temperature is not extremely high (approximately 310 K) at the level of millimeters. Therefore, the communication link with acceptable signal to noise ratio can exist within the human tissue in the Terahertz band.

### 3. Analysis of in-body communication capabilities

Nano-antennas generally support electromagnetic communications in the Terahertz band [20]. Therefore, the physical interface of a BANNET may use a bandwidth ranging from a few hundred of gigahertz to almost 10 THz. But the design of an efficient modulation scheme for Terahertz communications is not an easy task. In fact, due to the size and energy constraints of nano-machines, classical communication techniques based on the transmission of signals with long duration cannot be used in this context. On the contrary, considering the huge available bandwidth, it is preferable to encode the information by using short pulses spread on the whole bandwidth. By taking into account this important constraint, a promising modulation technique is the Time Spread On-Off Keying (TS-OOK), which ensures both high energy and communication effi-

210 ciency [10][29]. With TS-OOK, a logical 1 is encoded as a short pulse and a  
logical 0 is encoded as a silence. Moreover, due to technological limitations (i.e.,  
the communication unit can work only with a very low duty-cycle), the time  
between two consecutive pulses should be much longer than the pulse duration.  
TS-OOK offers two important advantages. From one side, it does not require  
215 synchronization among nano-devices before the transmission of a message. From  
another side, it also allows the sharing of the medium among multiple users. In  
fact, since the time between the transmission of two consecutive pulses has to  
be much longer than the pulse duration, several nano-devices can concurrently  
send sequences of pulses slightly time-shifted, without incurring in collisions.

220 Communication capabilities strongly depend on the frequency distribution of  
the transmitted power,  $P_{tx}$ . Moreover, in line with [20] and [15], three different  
communication schemes are taken into account for evaluating channel capacity  
and transmission ranges available in a BANNET. They are:

- 225 • **Flat communication:** it assumes that the total transmitted power is  
uniformly distributed over the entire operative bandwidth.
- **Pulse-based communication:** by taking into account the capabilities  
of graphene-based nanoelectronic, the pulse generated by a nano-machine,  
i.e., the wave form used to transmit the logical ‘1’, is modeled with a  $n$ -th  
derivative of a Gaussian-shape
- 230 • **Optimal communication:** it aims at maximizing the overall channel  
capacity by optimally adapting the power allocation as a function of  
frequency-selective properties of the channel.

Now, with reference to the channel model described in the previous Section  
and set of baseline transmission schemes summarized before, the communication  
235 capabilities (expressed in terms of channel capacity and related transmission  
ranges) of electromagnetic-based nanoscale communications in human tissues  
are analytically evaluated.

In line with [9, 11, 15, 20, 30, 29], the pulse energy and the pulse dura-



tion have been set to 500 pJ and 100 fs, respectively. Therefore, the resulting  
 240 transmitted peak power is equal to  $P_{tx} = 500 \text{ pJ}/100 \text{ fs} = 5 \text{ kW}$ . Moreover, the  
 considered operative bandwidth has been set to 1 THz, ranging from 0.5 THz to  
 1.5 THz. Finally, when the *pulse-based* transmission scheme is used, the deriva-  
 tive order and the standard deviation of the Gaussian pulse are set to 4 and  
 0.15, respectively.

245 First of all, in order to highlight the main difference between the transmis-  
 sion techniques described in the previous Section, their power spectral density  
 profiles have been depicted in Figure 9. As expected, when the *flat* transmission  
 scheme is used, the total power is uniformly distributed in the frequency domain  
 and the resulting power spectral density level is always equal to 5 nW/Hz per  
 250 sub-band. A slightly different behavior is provided by the *pulse-based* transmis-  
 sion scheme: its power spectral density profile follows a bell-shaped trend, which  
 reaches minimum values ( $= 2.81 \text{ nW/Hz}$ ) in the lower and higher portion of the  
 bandwidth and the maximum value ( $= 5.84 \text{ nW/Hz}$ ) around 1.07 THz. There  
 are two main comments emerging from analysis of the aforesaid transmission  
 255 techniques. From one side, the power profile does not change with the  
 distance between source and destination node. From another side, the power  
 is always distributed over the entire operative bandwidth, that is there are not  
 unused sub-bands. Completely different considerations can be done for the *opti-  
 mal* transmission scheme. The optimal strategy prefers to distribute the power  
 260 only to a subset of frequencies that experience better propagation conditions.  
 Therefore, in line with the path loss model reported in Figure 7, only the first  
 portion of the bandwidth is exploited for the transmission and the number of  
 used sub-bands decreases as the distance between source and destination node  
 increases (to provide a valid example, Figure 9 shows the optimal power profile  
 265 computed when the transmission distance is set to 2 mm and 3 mm).

Now, let  $P(\omega_i, \tilde{z})$  be the power spectral density that the generic transmission  
 sets for the  $i$ -th sub-band and when the distance between source and destination  
 node is equal to  $\tilde{z}$ . The Signal-to-Noise Ratio (SNR) measured for the  $i$ -th

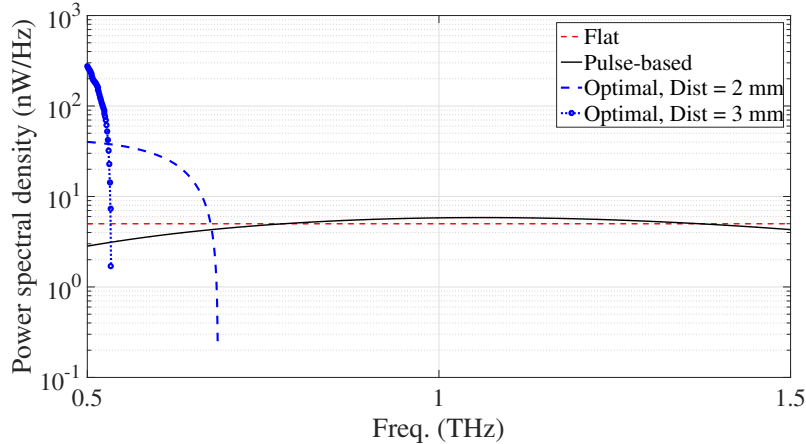


Figure 9: Power spectral densities of the considered transmission schemes.

sub-band at a distance  $\tilde{z}$  is equal to:  $\frac{P(\omega_i, \tilde{z})}{A(\omega_i, \tilde{z})N(\omega_i, \tilde{z})}$ . Figures 10, 11, and 12  
 270 report the SNR obtained when the *flat*, *pulse-based*, and *optimal* transmission  
 schemes are used, respectively. In this context, conducted tests demonstrate  
 that *flat* and *pulse-based* transmission schemes register an SNR that decreases  
 when both the distance between source and destination node and the frequency  
 increase. Of course, this result is completely in line with the path loss trend  
 275 already investigated in the previous Section. When the optimal scheme is used,  
 instead, two key aspects emerges. First, it is possible to note that the SNR  
 can be evaluated just of a sub set of frequencies, that are those used for the  
 transmission. Second, the adoption of the optimal power profile brings to SNR  
 values that slightly reduces with the distance between communicating nodes,  
 280 while maintaining similar values in the frequency domain.

To conclude, the upper bound of channel capacity in human tissues has been  
 estimated. For jointly considering technological constraints (specifically, the  
 inverse of the pulse duration) and the Shannon theorem, it has been evaluated  
 by:

$$C(\tilde{z}) = \min \left\{ \frac{1}{P_d}, \sum_i \Delta f \log_2 \left[ 1 + \frac{P(\omega_i, \tilde{z})}{A(\omega_i, \tilde{z})N(\omega_i, \tilde{z})} \right] \right\}. \quad (11)$$

Obtained results are reported in Figures 13-15, alongside the values of the

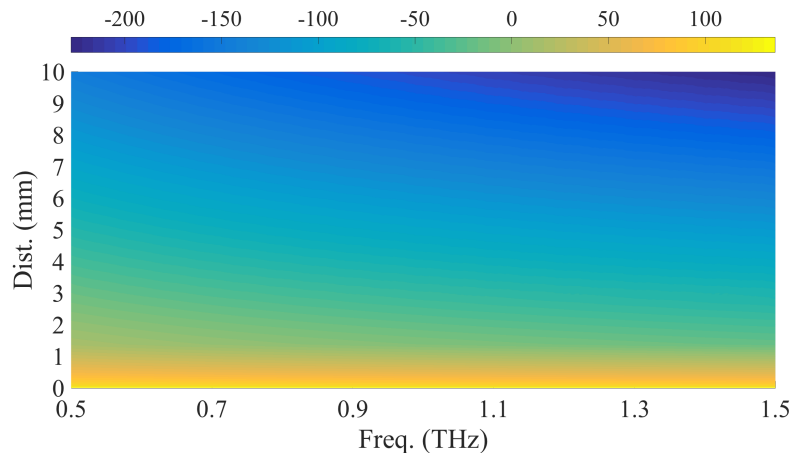


Figure 10: Calculated SNR concerning the flat transmission scheme.

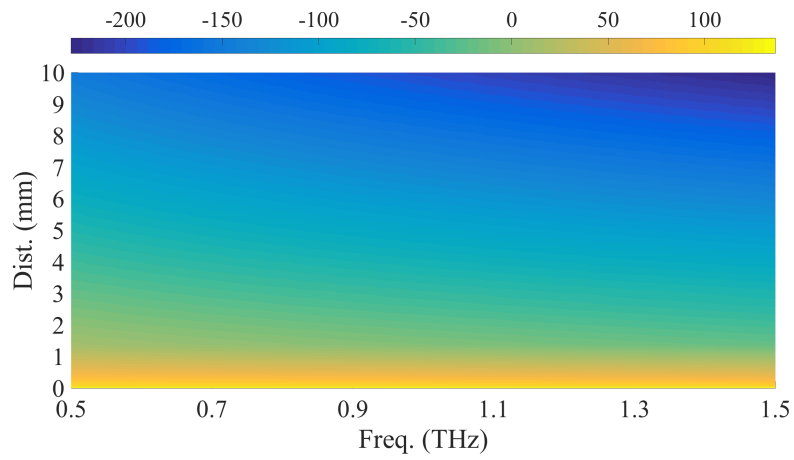


Figure 11: Calculated SNR concerning the pulse-based transmission scheme.

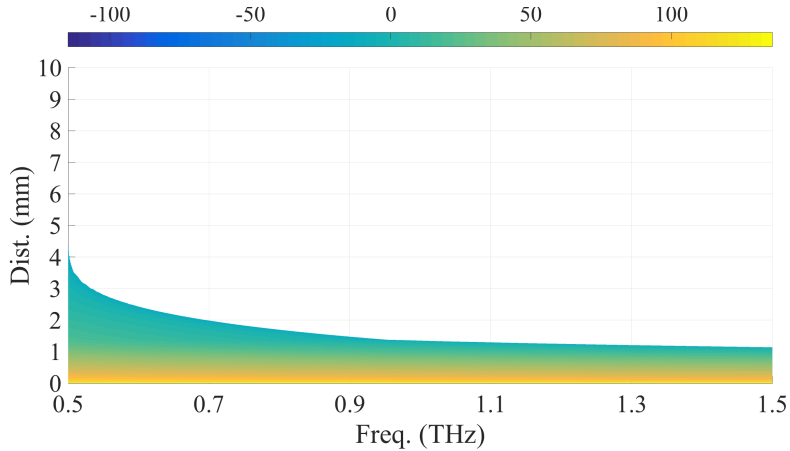


Figure 12: Calculated SNR concerning the optimal transmission scheme.

channel capacity available in the literature and referring to homogeneous media (see [11],[14], and [15]). As expected, the channel capacity decreases with the distance between source and destination node. Moreover, it is possible to observe that the *optimal* transmission scheme ensures the highest performance thanks to its ability to optimally adapt the power distribution in the frequency domain as a function of the attenuation level. On the other hand, the *pulse-based* approach registers the worst condition because it is not able to allocate a satisfactory amount of power in sub-channels experiencing the worst path loss.

From the obtained results, it is evident that a physical data rate in the order of Tbps can be only reached for transmission ranges less than 2 mm. Furthermore, when the distance between source node and destination device exceeds 9 mm, communication capabilities are extremely injured (i.e., the physical data rate becomes lower than 1 bps). Obtained results clearly confirms that the propagation of electromagnetic waves in human tissues is significantly impaired: the estimated channel capacity and the related communication ranges are notably reduced with respect to those achievable in the air medium. Moreover, differently from what discussed in [11],[14], and [15], our findings show more accurate performance indexes reachable in a BANNET. They, in fact, take care of the sig-

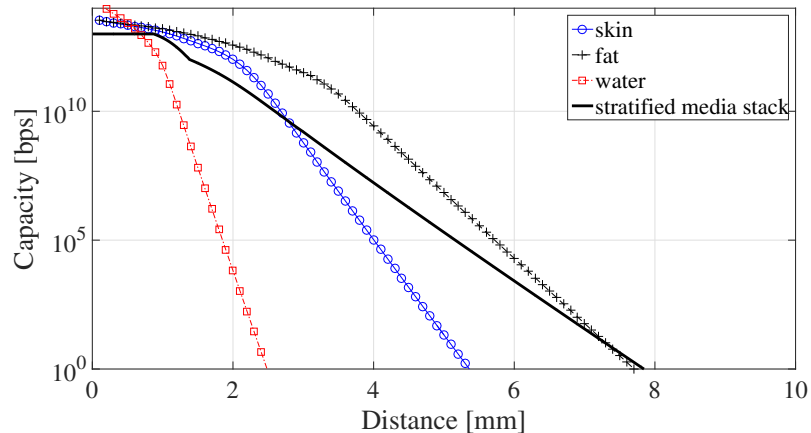


Figure 13: Channel capacity vs transmission ranges when the flat transmission scheme is used.

300 nal transmission in inhomogeneous human tissues modeled through a stratified medium stack.

#### 4. Conclusions

This paper investigated the propagation of Pulsed Electric Field in human tissues modeled with a stratified media stack made up by stratum corneum, epidermis, dermis, and fat. Indeed, starting from an accurate modeling of the electromagnetic problem, propagation losses and molecular absorption noise temperature have been calculated as a function of both frequency and communication distance. Then, reference transmission schemes, recently proposed in the literature, have been used for quantifying the upper bound of the channel capacity and related transmission ranges. Obtained results demonstrated that 310 Terahertz communications in human tissues are extremely challenging. Since the supported transmission ranges are very limited, the provisioning of advanced healthcare applications requires the development of effective Body Area Nano-NETworks, supporting multi-hop network topologies and sophisticated channel access schemes. In the future, we plan to further investigate the propagation 315 issues by also considering the possibility to locate source and destination node

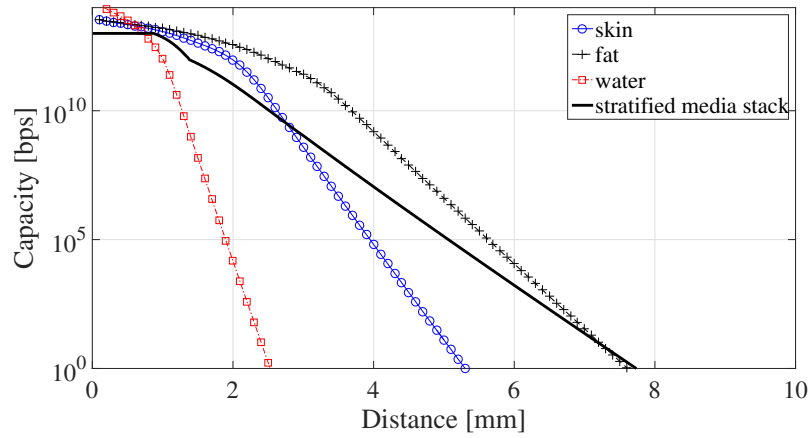


Figure 14: Channel capacity vs transmission ranges when the Gauss transmission scheme is used.

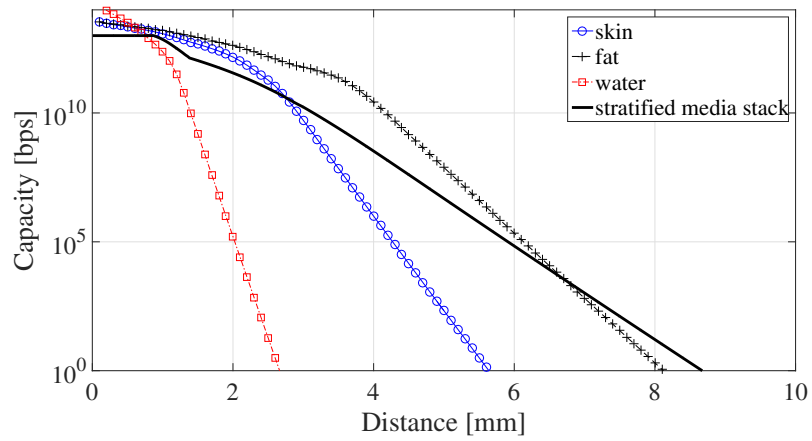


Figure 15: Channel capacity vs transmission ranges when the optimal transmission scheme is used.

inside and outside the human body, as well as to conceive novel networking solutions able to support specific applications in upcoming Body Area Nano-NETworks, trying to ensure the service also with the identified intrinsic physical limits.

## Appendix

To examine the behavior of the electromagnetic field propagation in dielectric materials, the integration of curl Maxwell's equations has to be performed:

$$\nabla \times \mathcal{H} = \frac{\partial \mathcal{D}}{\partial t} + \mathcal{J}_0 \quad (12)$$

$$\nabla \times \mathcal{E} = -\mu_0 \frac{\partial \mathcal{H}}{\partial t} \quad (13)$$

where  $\mathcal{D}$  is the electric displacement field,  $\mathcal{E}$  and  $\mathcal{H}$  are the electric and magnetic field, respectively,  $\mathcal{J}_0$  is the electromagnetic field source,  $\mu_0$  is the magnetic permeability of free space.

To calculate the spatial and temporal distributions of the electromagnetic fields in a generic dispersive medium, the constitutive relation between the electric and magnetic fields has to be combined with the equations 12-13. In a linear time-invariant medium, it can be written, in frequency domain, as:

$$\mathbf{D}(\omega) = \epsilon_0 \epsilon_r(\omega) \mathbf{E}(\omega), \quad (14)$$

where  $\epsilon_r$  is defined by Eq. (1),  $\mathbf{D}$  and  $\mathbf{E}$  are the Fourier transform of  $\mathcal{D}$  and  $\mathcal{E}$ , respectively.

Let us consider the following approximated fractional expansion:

$$\Gamma_p(j\omega\tau_p) = [1 + (j\omega\tau_p)^{\alpha_p}]^{\beta_p} \approx \sum_{n=0}^{K_{max,p}} \chi_{n,p} (j\omega\tau_p)^{\zeta_{n,p}}, \quad (15)$$

where the parameters  $0 \leq \chi_{n,p} \leq a$  and  $0 \leq \zeta_{n,p} \leq b$ , with  $a$  and  $b$  denoting assigned positive real numbers calculated by minimizing a suitable error function.

Upon substituting Eq. (15) in Eq. (14), and applying the inverse Fourier transform, it is straightforward to rewrite Eq. (12) as:

$$\nabla \times \mathcal{H} = \epsilon_0 \epsilon_{r\infty} \frac{\partial \mathcal{E}}{\partial t} + \sigma \mathcal{E} + \sum_{p=1}^N \mathcal{J}_p + \mathcal{J}_0, \quad (16)$$

where the  $k$ -th term of the auxiliary displacement current density,  $\mathcal{J}$ , is a solution of the equation:

$$\mathcal{D}_t^{(k)} \mathcal{J}_k = \epsilon_0 \Delta \epsilon_{r_k} \frac{\partial \mathcal{E}}{\partial t}. \quad (17)$$

Now, by replacing Eq. (17) in Eq. (16), it can be obtained

$$\nabla \times \mathcal{H} - \frac{\epsilon_{r\infty}}{\Delta \epsilon_{r_k}} \mathcal{D}_t^{(k)} \mathcal{J}_k = \sigma \mathcal{E} + \sum_{p=1}^N \mathcal{J}_p + \mathcal{J}_0. \quad (18)$$

Note that Eq. (18) involves the fractional derivative operator,  $\mathcal{D}_t^{(k)}$ , defined as:

$$\mathcal{D}_t^{(k)} = \mathcal{F}^{-1} \{ \Gamma_k(j\omega\tau_s) \} = \sum_{n=0}^{K_{max,k}} \chi_{n,k} \tau_k^{\zeta_{n,k}} D_t^{\zeta_{n,k}}, \quad (19)$$

330 where  $D_t^{\zeta_{n,k}}$  is the time derivative of fractional order  $\zeta_{n,k}$ .

By using the Riemann-Liouville definition of fractional derivative, the following equation is derived:

$$D_t^{\zeta_{n,k}} \mathcal{J}_k = \frac{d^\nu}{dt^\nu} \int_0^t \frac{(t-u)^{\nu-\zeta_{n,k}-1}}{\Gamma(\nu-\zeta_{n,k})} \mathcal{J}_k du \quad (20)$$

where  $\nu$  is an integer number such that  $\nu-1 \leq \zeta_{n,k} < \nu$  and  $\Gamma(\cdot)$  is the gamma function.

By setting

$$\mathcal{I}_{\zeta_{n,k}} = \int_0^t (t-u)^{\nu-\zeta_{n,k}-1} \mathcal{J}_k du \quad (21)$$

and considering the central finite difference approximation with time step  $\Delta t$ , Eq. (21) evaluated at the general time instant  $t = m\Delta t$  becomes

$$\begin{aligned} \mathcal{I}_{\zeta_{n,k}}|_m &\approx \sum_{l=0}^{m-1} \mathcal{J}_k|^{m-l-\frac{1}{2}} \int_{l\Delta t}^{(l+1)\Delta t} u^{\nu-\zeta_{n,k}-1} du \\ &\approx \frac{\Delta t^{\nu-\zeta_{n,k}}}{\nu-\zeta_{n,k}} \sum_{q=1}^{Q_{n,k}} a_q^{(\zeta_{n,k})} e^{-b_q^{(\zeta_{n,k})} l} \mathcal{J}_k|^{m-l-\frac{1}{2}} \end{aligned} \quad (22)$$



where

$$\sum_{q=1}^{Q_{n,k}} a_q^{(\zeta_{n,k})} e^{-b_q^{(\zeta_{n,k})} l} \approx (l+1)^{\nu-\zeta_{n,k}} - l^{\nu-\zeta_{n,k}} \quad (23)$$

By setting

$$\psi_q^{(\zeta_{n,k})} |^m = \sum_{l=0}^{m-1} a_q^{(\zeta_{n,k})} e^{-b_q^{(\zeta_{n,k})} l} \mathcal{J}_k |^{m-l-\frac{1}{2}} = a_q^{(\zeta_{n,k})} \mathcal{J}_k |^{m-\frac{1}{2}} + e^{-b_q^{(\zeta_{n,k})}} \psi_q^{(\zeta_{n,k})} |^{m-1} \quad (24)$$

Eq. (22) can be rewritten as:

$$\mathcal{I}_{\zeta_{n,k}} |^m \approx \frac{\Delta t^{\nu-\zeta_{n,k}}}{\nu-\zeta_{n,k}} \left[ A^{(\zeta_{n,k})} \mathcal{J}_k |^{m-\frac{1}{2}} + \sum_{q=1}^{Q_{n,p}} e^{-b_q^{(\zeta_{n,k})}} \psi_q^{(\zeta_{n,k})} |^{m-1} \right], \quad (25)$$

where

$$A^{(\zeta_{n,k})} = \sum_{q=1}^{Q_{n,k}} a_q^{(\zeta_{n,k})}. \quad (26)$$

Considering Eq. (20), the  $\nu$ th-order time-derivative of  $\mathcal{I}_{\zeta_{n,k}}$  calculated at the time instant  $t = m\Delta t$  can be approximated as:

$$\begin{aligned} \frac{d^\nu \mathcal{I}_{\zeta_{n,k}} |^m}{dt^\nu} &\approx \frac{1}{(\Delta t)^\nu} \sum_{s=0}^{\nu} (-1)^s \binom{\nu}{s} \mathcal{I}_{\zeta_{n,k}} |^{m-s+1} \\ &\approx \frac{\Delta t^{\nu-\zeta_{n,k}}}{\nu-\zeta_{n,k}} \left\{ A^{(\zeta_{n,k})} \left[ \mathcal{J}_k |^{m+\frac{1}{2}} + \sum_{s=1}^{\nu} (-1)^s \binom{\nu}{s} \mathcal{J}_k |^{m-s+\frac{1}{2}} \right] + \right. \\ &\quad \left. + \sum_{s=0}^{\nu} (-1)^s \binom{\nu}{s} \sum_{q=1}^{Q_{n,k}} e^{-b_q^{(\zeta_{n,k})}} \psi_q^{(\zeta_{n,k})} |^{m-s} \right\}. \quad (27) \end{aligned}$$

Moreover, Eq. (18) calculated at the time instant  $t = m\Delta t$  becomes

$$\nabla \times \mathcal{H} |^m - \frac{\epsilon_{r\infty}}{\Delta \epsilon_{r_k}} \mathcal{D}_t^{(k)} \mathcal{J}_k |^m = \sigma \mathcal{E} |^m + \sum_{p=1}^N \mathcal{J}_p |^m + \mathcal{J}_0 |^m, \quad (28)$$

and applying a second order accurate finite-difference scheme both electric and auxiliary displacement current fields can be written as

$$\mathcal{E} |^m = \frac{\mathcal{E} |^{m-\frac{1}{2}} + \mathcal{E} |^{m+\frac{1}{2}}}{2} \quad (29)$$

$$\mathcal{J}_p |^m = \frac{\mathcal{J}_p |^{m-\frac{1}{2}} + \mathcal{J}_p |^{m+\frac{1}{2}}}{2}. \quad (30)$$

In addition,

$$\begin{aligned}
\mathcal{D}_t^{(k)} \mathcal{J}_k |^m &= \sum_{n=0}^{K_{max,k}} \chi_{n,k} \tau_k^{\zeta_{n,k}} \frac{d^\nu \mathcal{I}_{\zeta_{n,k}}}{dt^\nu} |^m \\
&= C^{(\zeta_{n,k})} \mathcal{J}_k |^{m+\frac{1}{2}} + \sum_{n=0}^{K_{max,k}} \sum_{s=1}^{\nu} \xi_{n,s}^{(\zeta_{n,k})} \mathcal{J}_k |^{m-s+\frac{1}{2}} + \\
&+ \sum_{n=0}^{K_{max,k}} \sum_{s=1}^{\nu} \sum_{q=1}^{Q_{n,k}} \eta_{n,s,q}^{(\zeta_{n,k})} \psi_q^{(\zeta_{n,k})} |^{m-s}, \tag{31}
\end{aligned}$$

where

$$C^{(\zeta_{n,k})} = \sum_{n=0}^{K_{max,k}} \frac{\chi_{n,k} \tau_k^{\zeta_{n,k}} (\Delta t)^{\nu-\zeta_{n,k}}}{\nu - \zeta_{n,k}} A^{(\zeta_{n,k})} \tag{32}$$

$$\xi_{n,s}^{(\zeta_{n,k})} = (-1)^s \binom{\nu}{s} \frac{\chi_{n,k} \tau_k^{\zeta_{n,k}} (\Delta t)^{\nu-\zeta_{n,k}}}{\nu - \zeta_{n,k}} A^{(\zeta_{n,k})} \tag{33}$$

$$\eta_{n,s,q}^{(\zeta_{n,k})} = \frac{e^{-b_q^{(\zeta_{n,k})}}}{A^{(\zeta_{n,k})}} \xi_{n,s}^{(\zeta_{n,k})} \tag{34}$$

By using Eqs. (29)-(34), Eq. (28) can be rewritten as:

$$\begin{aligned}
&\left[ \left( \epsilon_{r_\infty} + \frac{\sigma \Delta t}{2\epsilon_0} \right) \frac{C^{(\zeta_{n,k})}}{\Delta \epsilon_{r_k}} + \frac{1}{2} \right] \mathcal{J}_k |^{m+\frac{1}{2}} + \frac{1}{2} \sum_{p=1, p \neq k}^N \mathcal{J}_p |^{m+\frac{1}{2}} = \\
&= (\nabla \times \mathcal{H}) |^m - \sigma \mathcal{E} |^{m-\frac{1}{2}} - \frac{1}{2} \sum_{p=1}^N \mathcal{J}_p |^{m-\frac{1}{2}} - \mathcal{J}_0 |^m - \frac{1}{\Delta \epsilon_{r_k}} \left( \epsilon_{r_\infty} + \frac{\sigma \Delta t}{2\epsilon_0} \right) \\
&\cdot \left[ \sum_{n=0}^{K_{max,k}} \sum_{s=1}^{\nu} \xi_{n,s}^{(\zeta_{n,k})} \mathcal{J}_k |^{m-s+\frac{1}{2}} + \sum_{n=0}^{K_{max,k}} \sum_{s=0}^{\nu} \sum_{q=1}^{Q_{n,\alpha_k}} \eta_{n,s,q}^{(\zeta_{n,k})} \psi_q^{(\zeta_{n,k})} |^{m-s} \right]. \tag{35}
\end{aligned}$$

Finally, the update equations for the electric field,  $\mathcal{E}$ , and the magnetic field,  $\mathcal{H}$  are:

$$\begin{aligned}
\mathcal{E} |^{m+\frac{1}{2}} &= \frac{2\epsilon_0 \epsilon_{r_\infty} - \sigma \Delta t}{2\epsilon_0 \epsilon_{r_\infty} + \sigma \Delta t} \mathcal{E} |^{m-\frac{1}{2}} + \frac{2\Delta t}{2\epsilon_0 \epsilon_{r_\infty} + \sigma \Delta t} \left[ (\nabla \times \mathcal{H}) |^m + \right. \\
&\left. - \frac{1}{2} \sum_{p=1}^N \left( \mathcal{J}_p |^{m-\frac{1}{2}} + \mathcal{J}_p |^{m+\frac{1}{2}} \right) \right], \tag{36}
\end{aligned}$$

$$\mathcal{H} |^{m+1} = \mathcal{H} |^m - \frac{\Delta t}{\mu_0} (\nabla \times \mathcal{E}) |^{m+\frac{1}{2}}. \tag{37}$$

## References

- [1] J. Caldeira, J. Rodrigues, P. Lorenz, Toward ubiquitous mobility solutions  
335 for body sensor networks on healthcare, *IEEE Communications Magazine*  
50 (5) (2012) 108–115.
- [2] S. Movassaghi, M. Abolhasan, J. Lipman, D. Smith, A. Jamalipour, Wire-  
less body area networks: A survey, *IEEE Communications Surveys Tuto-  
rials* 16 (3) (2014) 1658–1686.
- [3] M. ul Huque, K. Munasinghe, A. Jamalipour, Body node coordinator place-  
340 ment algorithms for wireless body area networks, *IEEE Internet of Things*  
*Journal* 2 (1) (2015) 94–102.
- [4] T. Nakano, M. Moore, F. Wei, A. Vasilakos, J. Shuai, Molecular communi-  
cation and networking: Opportunities and challenges, *IEEE Transactions*  
345 *on NanoBioscience* 11 (2) (2012) 135–148.
- [5] I. F. Akyildiz, J. M. Jornet, C. Han, Terahertz band: Next frontier for  
wireless communications, *Physical Communication* 12 (2014) 16–32.
- [6] I. Akyildiz, J. Jornet, Electromagnetic wireless nanosensor networks, *Nano*  
*Communication Networks* 1 (1) (2010) 3–19.
- [7] G. Santagati, T. Melodia, L. Galluccio, S. Palazzo, Medium access control  
350 and rate adaptation for ultrasonic intrabody sensor networks, *IEEE/ACM*  
*Transactions on Networking* 23 (4) (2015) 1121–1134.
- [8] B. Atakan, O. Akan, S. Balasubramaniam, Body area nanonetworks with  
molecular communications in nanomedicine, *IEEE Communications Mag-  
355 azine* 50 (1) (2012) 28–34.
- [9] G. Piro, G. Boggia, L. A. Grieco, On the design of an energy-harvesting  
protocol stack for Body Area Nano-NETworks, *Nano Communication Net-  
works Journal, Elsevier* 6 (2) (2015) 74–88.

- [10] J. Jornet, I. Akyildiz, Information capacity of pulse-based wireless nanosen-  
360 sor networks, in: Proc. of IEEE Conf. on Sensor, Mesh and Ad Hoc Com-  
munications and Networks, SECON, 2011, pp. 80–88.
- [11] Bush, J. Paluh, G. Piro, V. Rao, V. Prasad, A. Eckford, Defining commu-  
nication at the bottom, IEEE Transactions on Molecular, Biological, and  
Multi-Scale Communications (T-MBMC) 1 (1) (2015) 90–96.
- [12] J. M. Jornet, I. F. Akyildiz, Femtosecond-long pulse-based modulation for  
365 terahertz band communication in nanonetworks, IEEE Trans. on Commun.  
62 (5) (2014) 1742–1754.
- [13] P. Boronin, V. Petrov, D. Moltchanov, Y. Koucheryavy, J. M. Jornet,  
Capacity and throughput analysis of nanoscale machine communication  
370 through transparency windows in the terahertz band, Nano Communica-  
tion Networks 5 (3) (2014) 72–82.
- [14] K. Yang, A. Pellegrini, M. Munoz, A. Brizzi, A. Alomainy, Y. Hao, Numerical  
Analysis and Characterization of THz Propagation Channel for Body-  
Centric Nano-Communications, IEEE Transactions on Terahertz Science  
375 and Technology 5 (3) (2015) 419–426.
- [15] G. Piro, K. Yang, G. Boggia, N. Chopra, L. A. Grieco, A. Alomainy, Ter-  
ahertz communications in human tissues at the nano-scale for healthcare  
applications, IEEE Transactions on Nanotechnology 14 (3) (2015) 404–406.
- [16] H. Guo, P. Johari, J. M. Jornet, Z. Sun, Intra-body optical channel  
380 modeling for in vivo wireless nanosensor networks, IEEE Transactions on  
NanoBioscience 15 (1) (2016) 41–52.
- [17] S. J. Beebe, Bioelectrics in basic science and medicine: Impact of electric  
fields on cellular structures and functions, J. Nanomed. Nanotechol. 4 (2).
- [18] S. Corovic, I. Lackovic, P. Sustaric, T. Sustar, T. Rodic, D. Miklavcic, Mod-  
385 eling of electric field distribution in tissues during electroporation, BioMed-  
ical Engineering 12 (2013) 2–27.

- [19] A. T. Esser, K. C. Smith, T. R. Gowrishankar, J. C. Weaver, Towards solid tumor treatment by nanosecond pulsed electric fields, *Technology in Cancer Research and Treatment* 8 (2009) 289–306.
- 390 [20] J. Jornet, I. Akyildiz, Channel modeling and capacity analysis for electromagnetic wireless nanonetworks in the terahertz band, *IEEE Transactions on Wireless Communications* 10 (10) (2011) 3211–3221.
- [21] L. Mescia, P. Bia, D. Caratelli, Fractional derivative based FDTD modeling of transient wave propagation in Havriliak-Negami media, *IEEE Trans. Microwave Theory and Techniques* 62 (2014) 1920–1929.
- 395 [22] P. Bia, D. Caratelli, L. Mescia, R. Cicchetti, G. Maione, F. Prudenzano, A novel FDTD formulation based on fractional derivatives for dispersive Havriliak-Negami media, *Signal Processing* 107 (2014) 312–318.
- [23] L. Mescia, P. Bia, D. Caratelli, Fractional-calculus-based FDTD method for solving pulse propagation problems, in: *IEEE International Conference on Electromagnetics in Advanced Applications (ICEAA)*, 2015, pp. 460–463.
- 400 [24] S. Alekseev, M. Ziskin, Human Skin Permittivity Determined by Millimeter rWave Reflection Measurements, *Bioelectromagnetics* 28 (2007) 331–339.
- [25] K. Sasaki, M. Mizuno, K. Wake, S. Watanabe, Measurement of the dielectric properties of the skin at frequencies from 0.5 GHz to 1 THz using several measurement systems, in: *International Conference on Infrared, Millimeter, and Terahertz waves (IRMMW-THz)*, Hong Kong, 2015.
- 405 [26] M. Ney, I. Abdulhalim, Does human skin truly behave as an array of helical antennae in the millimeter and terahertz wave ranges?, *Optics Letters* 35 (2010) 3180–3182.
- 410 [27] S. Naito, M. Hoshi, S. Yagihara, Microwave dielectric analysis of human stratum corneum in vivo, *Biochimica et Biophysica Acta* 1381 (1998) 293–304.

- [28] P. Hasgall, F. D. Gennaro, C. Baumgartner, E. Neufeld, M. Gosselin,  
415 D. Payne, A. Klingebck, N. Kuster, ITIS database for thermal and elec-  
tromagnetic parameters of biological tissues (2015).  
URL <http://www.itis.ethz.ch/database>
- [29] J. M. Jornet, I. F. Akyildiz, Graphene-based plasmonic nano-antenna for  
420 terahertz band communication in nanonetworks, *IEEE Journal on Selected  
Areas in Communications* 31 (12) (2013) 685–694.
- [30] J. Jornet, I. Akyildiz, Joint energy harvesting and communication analysis  
for perpetual wireless nanosensor networks in the terahertz band, *IEEE  
Transactions on Nanotechnology* 11 (3) (2012) 570–580.